Direct Numerical Simulation of a Supercritical Planar Jet

Leandro B. Magalhães*†¶‡ and Marco Zecchetto* and André R. Silva¶ and Carlos B. da Silva*
*IDMEC, Instituto Superior Técnico, Universidade of Lisbon, Lisbon 1049-001, Portugal

¶ AEROG-LAETA University of Beira Interior, Covilhã 6201-001, Portugal

‡ ISEC Lisbon Institute for Education and Sciences, Lisbon 1750-142, Portugal
leandro.magalhaes@tecnico.ulisboa.pt· marco.zecchetto@tecnico.ulisboa.pt·
andre@ubi.pt· carlos.silva@tecnico.ulisboa.pt

†Corresponding author

Abstract

The proposed manuscript reports on the development of a DNS low-Mach flow solver for the evaluation of supercritical fluid flows at conditions relevant to aero-propulsive systems such as liquid rocket and gas turbine engines. Validation is carried out through comparison with experimental data of constant-density jets, while the results are going to report the visualization of turbulence coherent structures at variable-density conditions and an evaluation of the physical mechanisms taking place at the turbulent/non-turbulent (T/NT) interface.

1. Introduction

The lack of quantitative experimental data on the density and temperature fields and turbulence statistics on supercritical fluid flow behaviuor allied with the high cost of experimental campaigns paves the way for the use of detailed direct numerical simulation techniques of turbulent jets of supercritical fluid conditions. At such conditions a mixing layer forms naturally due to the interaction between a central stream jet and a co-flowing one, with relative parallel velocities. Furthermore, under these variable density conditions, characteristic of those encountered in the operation of liquid propelled rocket engines, the mixing characteristics also depend upon the density ratio. These are similar to the behaviour of a jet in its mixing region. Several research groups focused on the study of supercritical fluid injection phenomena, dealing with real fluid mixing layers.

The supercritical fluid jet modelling^{14,15} is usually validated against the small number of quantitative experimental data sets available.^{9,18} These expensive experimental campaigns resulted from state-funded research programs at the American Air Force Research Laboratory and the German DLR. However, since they came into being, much has changed at the scientific and political levels. From a scientific point of view, knowledge regarding supercritical fluid flows has evolved since the experimental campaigns were carried out – heat transfer in injectors, neglected from an experimental standpoint, was found to be of paramount importance for jet evolution, first under supercritical gas-like conditions,² where no dense potential core was formed, and more recently¹⁵ at supercritical liquid-like conditions where shorter potential cores were obtained.

Traditionally these flows have been studied through the use of fully compressible formulations.²⁰ However, the Mach number of such flows is very low, due to the low velocity at which injection takes place. Allied with the high speed of sound, it will impose severe time step constraints on the numerical simulations.¹ The alternative is to employ low-Mach number approximations, ^{1,3,23} where pressure and density are decoupled through the use of an EoS for density, neglecting compressibility and acoustic effects, which are filtered *a priori*. Low-Mach number approximations have also been employed in the context of turbulent combustion due to the possibility of removing acoustic effects.¹⁶

Without considering the compressibility effects, it is possible to determine all thermodynamic state variables, such as density and enthalpy, independently of the hydrodynamic pressure variations about a specified background or thermodynamic pressure. This is equivalent to say that the heat transfer process we are now considering is a thermodynamically constant-pressure process, which is a typical assumption for most of heat transfer problems in low-speed incompressible flows. In the present study, we also neglect viscous dissipation and gravitational work terms in the energy equation because their effects are generally very small in low-speed flows. Such an approach is suitable to describe incompressible but variable density behavior, decoupling pressure, and density (defined through a real fluid equation of state). Such as a process of the compressible but variable density behavior, decoupling pressure, and density (defined through a real fluid equation of state).

The primary objective of this paper is to report on the development and validation of a numerical tool capable of performing direct numerical simulations (DNS) of temporal jets for both incompressible- and variable-density cases.

The impact of variable density on flow structures and turbulence statistics is systematically analysed and compared to the incompressible case. Differences in small-scale structures, energy spectra, and other statistical quantities are evaluated to gain insights into how density variations influence turbulence dynamics.

The remaining of this manuscript is organized as follows: the mathematical methods are discussed in 2, focusing on the low-Mach number approach governing equations. Then, a summary of the numerical solver is given in 3 detailing discretization schemes, stability conditions and a brief explanation of conditional statistics determination across the turbulent/non-turbulent interface. Finally, numerical results detailing constant- and variable-density jets are depicted in 4, and the main findings are summarized in 5.

2. Mathematical and Physical Models

Conservation equations for mass, momentum, and energy as well as the ideal gas equation as given in equations (1) to (4). The equations are written in dimensionless form, where ρ is the density, t the time, u the velocity, x the space coordinate, σ the shear stress tensor, γ the adiabatic index, T the temperature, Fr the Froude number, Re the Reynolds number and Pr the Prandtl number.

$$\frac{\partial \rho^{(0)}}{\partial t} + \frac{\partial \rho^{(0)} u_j^{(0)}}{\partial x_i} = 0 \tag{1}$$

$$\frac{\partial \rho^{(0)} u_i^{(0)}}{\partial t} + \frac{\partial \rho^{(0)} u_i^{(0)} u_j^{(0)}}{\partial x_i} = -\frac{\partial \rho^{(1)}}{\partial x_i} + \frac{\rho^{(0)}}{Fr} \gamma_i + \frac{1}{Re} \frac{\partial \sigma_{ij}^{(0)}}{\partial x_i}$$
(2)

$$\rho^{(0)}T^{(0)}\frac{\partial u_j^{(0)}}{\partial x_i} = \frac{1}{\text{RePr}}\frac{\partial}{\partial x_i} \left(\mu \frac{\partial T^{(0)}}{\partial x_i}\right) \tag{3}$$

$$p^0 = \rho^{(0)} T^{(0)} \tag{4}$$

Viscous dissipation and gravitational work terms in the energy equation are neglected because their effects are generally very small in low-speed flows. Such an approach is suitable to describe incompressible but variable density behaviour, decoupling pressure and density.

Initial temperature, velocity and passive scalar profiles are imposed at the inlet following hyperbolic-tangent profiles, while density is retrieved from the equation of state. As preliminary results, we highlight the vorticity field in the attachment during the early stages of transition.

3. Numerical Methods

3.1 Numerical Solver

An in-house DNS code is being continuously developed^{6,17} capable of carrying out DNS of temporal jets and homogenous isotropic turbulence. A spectral method is used to compute spatial derivatives and a second-order Adams-Bashforth time-stepping scheme is used to advance the simulation in time. Additionally, a pressure correction step is performed to satisfy the continuity equation.

$$U^{n+1} - U^n = \Delta t \left(3H^n - H^{n-1} \right) \frac{1}{2} \tag{5}$$

The spatial derivatives are evaluated in the Fourier space, where fast Fourier transforms (FFT) are used to change between the physical and the Fourier space.

The local temporal derivatives of density are obtained by applying the product rule to the second term of the mass conservation equation (equation (1)) and substituting in the energy conservation equation (equation (3)) we can predict density at the next instant using Adams-Bashforth temporal integration:

$$\rho^{n+1} - \rho^n = \Delta t \left(\frac{3}{2} \frac{\partial \rho}{\partial t} \Big|^n - \frac{1}{2} \frac{\partial \rho}{\partial t} \Big|^{n-1} \right)$$
 (6)

Temperature for instant n + 1 can be calculated directly from the ideal gas equation of state as:

$$p^0 = 1 = \rho^{n+1} T^{n+1} \tag{7}$$

An intermediate velocity field, \hat{u}_i^p is obtained using the pressure-plit momentum equations:

$$\rho^{n+1}\hat{u}_i^p - \rho^n u_i^n = \Delta t \left(\frac{3}{2} R_i^n - \frac{1}{2} R_i^{n-1} \right)$$
 (8)

Where the right-hand side of the Navier-Stokes equations, R_i , is given by:

$$R_{i} = -\frac{\partial \rho u_{i} u_{j}}{\partial x_{j}} + \frac{\rho}{Fr} \delta_{1i} + \frac{1}{Re} \frac{\partial \sigma_{ij}}{\partial x_{j}}$$

$$\tag{9}$$

The intermediate pressure term, p^* is retrieved through the inversion of the Poisson type pressure equation:

$$\frac{\partial^2 p^*}{\partial x_j^2} = \frac{1}{\Delta t} \left(\frac{\partial \rho^* \hat{u}_j^p}{\partial x_j} + \frac{\partial \rho}{\partial t} \right|^* \right) \tag{10}$$

where the term $\frac{\partial \rho}{\partial t}\Big|^*$ can be estimated through a second-order discretization:

$$\left. \frac{\partial \rho}{\partial t} \right|^* = \frac{1}{2\Delta t} \left(3\rho^* - 4\rho^n + \rho^{n-1} \right) \tag{11}$$

Finally, the velocity components for the next step can be calculated using a projection step:

$$\frac{\rho^* u_j^f - \rho^* \hat{u} j^p}{\Delta t} = -\frac{\partial p^*}{\partial x_j} \tag{12}$$

If only the predictor step is used, $u^f = u^{n+1}$, corresponding to the predicted velocity for time step t_{n+1} .

For the variable density simulations a corrector step was added to the numerical code. The value of density at time step t_{n+1} is estimated using a second-order quasi Crank-Nicholson integration:

$$\frac{\rho n + 1 - \rho^n}{\Delta t} = \frac{1}{2} \left(\frac{\partial \rho}{\partial t} \Big|^n + \frac{\partial \rho}{\partial t} \Big|^{**} \right)$$
 (13)

or:

$$\rho^{n+1} = \rho^* + \frac{1}{2\Delta t} \left(\frac{\partial \rho}{\partial t} \Big|^n + \frac{\partial \rho}{\partial t} \Big|^{**} \right)$$
 (14)

 $\frac{\partial \rho}{\partial t}\Big|^{**}$ is obtained by substituting the final velocity of the predictor step into equation (3). Moreover, a second intermediate velocity field, \hat{u}^c is determined using the pressure-split momentum equation defined by:

$$\rho^{n+1}\hat{u}_i^c - \rho^n u_i^n = \Delta t \left(\frac{3}{2} R_i^n - \frac{1}{2} R_i^{n-1} \right) \tag{15}$$

The predicted pressure field at time instant t_{n+1} is obtained with a Poisson-type equation:

$$\frac{\partial^2 p^*}{\partial x_i^2} = \frac{1}{\Delta t} \left(\frac{\partial \rho^* \hat{u}_j^c}{\partial x_j} \frac{\partial \rho}{\partial t} \right|^* \right) \tag{16}$$

with:

$$\left. \frac{\partial \rho}{\partial t} \right|^{n+1} = \frac{1}{2\delta t} \left(3\rho^{n+1} - 4\rho^n + \rho^{n+1} \right) \tag{17}$$

Lastly, the final velocity at time step t_{n+1} can be determined from equation (12).

The boundary conditions are ultimately dictated by the Fourier method, therefore are periodic in the three directions. The initial mean velocity field and the temperature fields are prescribed by a similar hyperbolic tangent profile in the streamwise component and is null in the other directions. The hyperbolic tangent is expressed as a function of the normal coordinate y translated of a $L_{\nu}/2$ distance from the origin:

$$\langle u(x, y, z, 0) \rangle = \frac{U_1 + U_2}{2} + \frac{U_1 - U_2}{2} \tanh \left[\frac{H}{4\theta_0} \left(1 - \frac{2|y - L_y/2|}{H} \right) \right]$$
 (18)

where θ_0 is the initial momentum thickness, and U_1 and U_2 are the maximum and minimum initial mean velocities respectively. To promote the transition to turbulence and therefore reducing the total computational time, a three-component velocity fluctuating spectral noise is superimposed to the hyperbolic tangent profile.⁸

3.2 Stability

A numerical method is considered to be stable if errors are not amplified during the system of partial differential equations computation. In spectral methods, stability pertains to whether small numerical errors introduced during the computations remain bounded as the solution evolves in time. In this sense, the Courant-Friedrichs-Lewy (CFL) number, determined as the ratio between the time step (Δt) over the characteristic convection time ($\Delta x/u$) is frequently used to determine the limiting time step to guarantee numerical stability at each iteration (equation (19)).

$$\Delta t = C_{max} \min\left(\frac{\Delta x}{|u|_{max}}, \frac{\Delta y}{|v|_{max}}, \frac{\Delta z}{|w|_{max}}\right)$$
(19)

With $|u|_{max}$, $|v|_{max}$ and $|w|_{max}$ being the maximum velocity in each direction and C_{max} a value chosen to obtain Δt for each time step.

3.3 Conditional Statistics

Conditional statistics are used to analyse physical variables based on their distance from a specific surface.²⁶ While this method is primarily tailored to study the turbulent/non-turbulent interface (TNTI), its application is broader and suitable for any scenario requiring data grouping by proximity to a surface or reference points.

The method relies on three primary geometrical components:

- 1. A defined reference surface (or a set of points);
- 2. Surface-normal vectors at each location;
- 3. A range of distances measured from the surface.

This approach is particularly important because conventional statistical methods - based on fixed spatial positions - fail to resolve the localized behaviours within the TNTI layer. This is due to its irregular and fluctuating shape, which causes standard measurements to mix data from turbulent and non-turbulent regions, thus obscuring fine-scale dynamics.

To compute these conditional statistics, a three-step process is followed²⁴ (Figure 1):

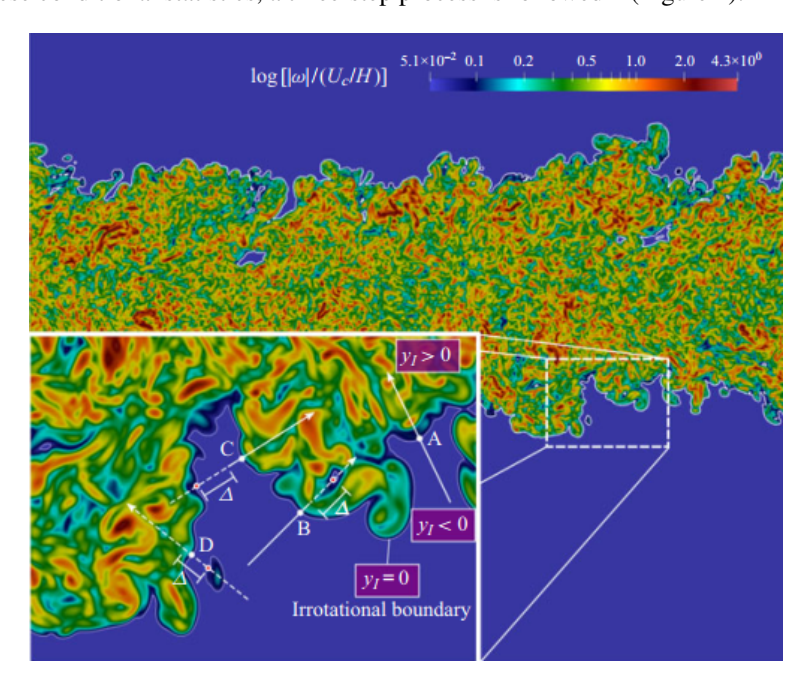


Figure 1: Sketch of the procedure used to compute the conditional statistics in relation to the position of the IB or the interface enveloping the IB, showing contours of enstrophy in a (x,y) plane.²⁴

1. Detection of the Irrotational Boundary (IB): The initial step involves identifying the outer edge of the turbulent region - known as the IB - by locating an isosurface characterized by low vorticity magnitude. This is achieved by analysing the distribution of the turbulent fraction of the flow.

- 2. Computation of Local Normals: After the IB is established, the gradient of enstrophy is utilized to determine three-dimensional normal vectors at each point on the surface, particularly within the upper and lower shear layers that bound the interface.
- 3. Data Sampling Along Normals: With these normal vectors, relevant flow quantities are extracted at specified distances (denoted by y_I) along the normals using trilinear interpolation. These distances define relative positions to the IB: $y_I = 0$ corresponds to the boundary, $y_I < 0$ lies on the irrotational side, and $y_I > 0$ is within the turbulent region. The conditional average of any flow variable ϕ under this framework is represented by $\langle \phi \rangle_I$.

4. Results

Using the DNS code presented in the previous section, we carried out three direct numerical simulations with parameters reported in Table 4. In this table: $(N_x \times N_y \times N_z)$ denotes the number of collocation points used in the stream-wise (x), normal (y), and span-wise (z) directions, respectively; $(L_x \times L_y \times L_z)$ represents the size of the computational domain in these directions, expressed in units of the initial jet slot width; Re_H is the initial Reynolds number for the temporal jet simulations; and dT_1dT_2 is the temperature ratio between the central and outer regions.

Table 1: Summary of the temporal direct simulations of planar jets carried out for the present analysis.

dT_1dT_2	$(N_x \times N_y \times N_z)$	$(L_x \times L_y \times L_z)$	Re_H
1	$256 \times 256 \times 256$	$6H \times 6H \times 6H$	3000
2	$256 \times 256 \times 256$	$6H \times 6H \times 6H$	3000
4	$256 \times 256 \times 256$	$6H \times 6H \times 6H$	3000

4.1 Isothermal Jet

The analysis of classical mean fields and statistical moments is a critical step following the development of a DNS code, primarily for validation purposes.

To ensure meaningful comparisons, fields sufficiently far downstream were chosen so that the non-dimensional profiles collapse onto a single curve independently of the stream-wise coordinate (or time), indicating a self-similar behaviour. The classical theory of turbulent free shear flow formulates the self-similarity in the far field noticing that the dimensions of the eddies at a certain distance from the inlet are influenced by the local length scale representative of the turbulent region width at that location.

Self-similarity, by definition, exists when the non-dimensional profiles depend solely on a single non-dimensional parameter. For instance the mean velocity profile in the self-similar region can be expressed as:

$$\langle u(x, y, z) \rangle = U_c f(\xi) \text{ where } f(\xi) = \text{sech}^2 [0.5 \cdot \ln(1 + \sqrt{2})^2 x]$$
 (20)

where $U_c = \langle u(x,0,0) \rangle$ and $\xi = y/\delta_{0.5}$ with $\delta_{0.5}$ being the jet half width defined as the distance from the centre line in the to the point where $u(x,y,0) = U_c/2$. Thus, the self-similar profile $f(\xi)$, is independent of the stream-wise distance. Care must be taken, as jet spreading near the periodic boundaries can lead to confinement effects, especially at later times.

Figure 2 presents the profiles of the mean axial velocity and four components of the Reynolds stress rescaled by the centre line velocity to recover the self similar profile. The present DNS result $(dT_1dT_2 = 1)$ are compared with experiments results.^{4,5,10-13,19,22,25} The profiles presented here were obtained by averaging the flow variables across the fields in the homogeneous flow directions (specifically along the x and z axes). Afterward, these profiles were symmetrically folded along the centreline of the flow domain to enhance the statistical convergence of the results. This folding procedure ensures that the profiles exhibit improved statistical reliability by averaging over the entire domain. The degree of convergence observed in these simulations is quite similar to that typically seen in temporal planar jet simulations, suggesting that the approach is consistent with established methods in the field.

The mean velocity profiles, as well as the stream-wise Reynolds stress profiles, demonstrate a commendable level of agreement with both experimental measurements and available numerical data from other studies. This is particularly noteworthy because it indicates that not only are the large-scale motions well-resolved, but also the small-scale turbulence and fluctuations, represented by the velocity fluctuation profiles, are effectively captured. This dual resolution of both large and small scales is essential for an accurate representation of the turbulence dynamics in the system.

Moreover, the capability of the new planar jet simulations to resolve the small scales of motion is further highlighted by the three-dimensional kinetic energy spectra, as shown in Figure 4. The spectra for all simulations exhibit a clear inertial range with a slope close to the -5/3 law, followed by a smooth decay at higher wave numbers. This behaviour is characteristic of fully developed turbulence, and the fact that it is observed here reinforces the idea that the small-scale motions are being properly resolved. In all cases, the energy spectra demonstrate that the simulations successfully capture both the large-scale and small-scale turbulence dynamics, as requested in direct numerical simulations, validating the accuracy and robustness of the new temporal simulation methodology.

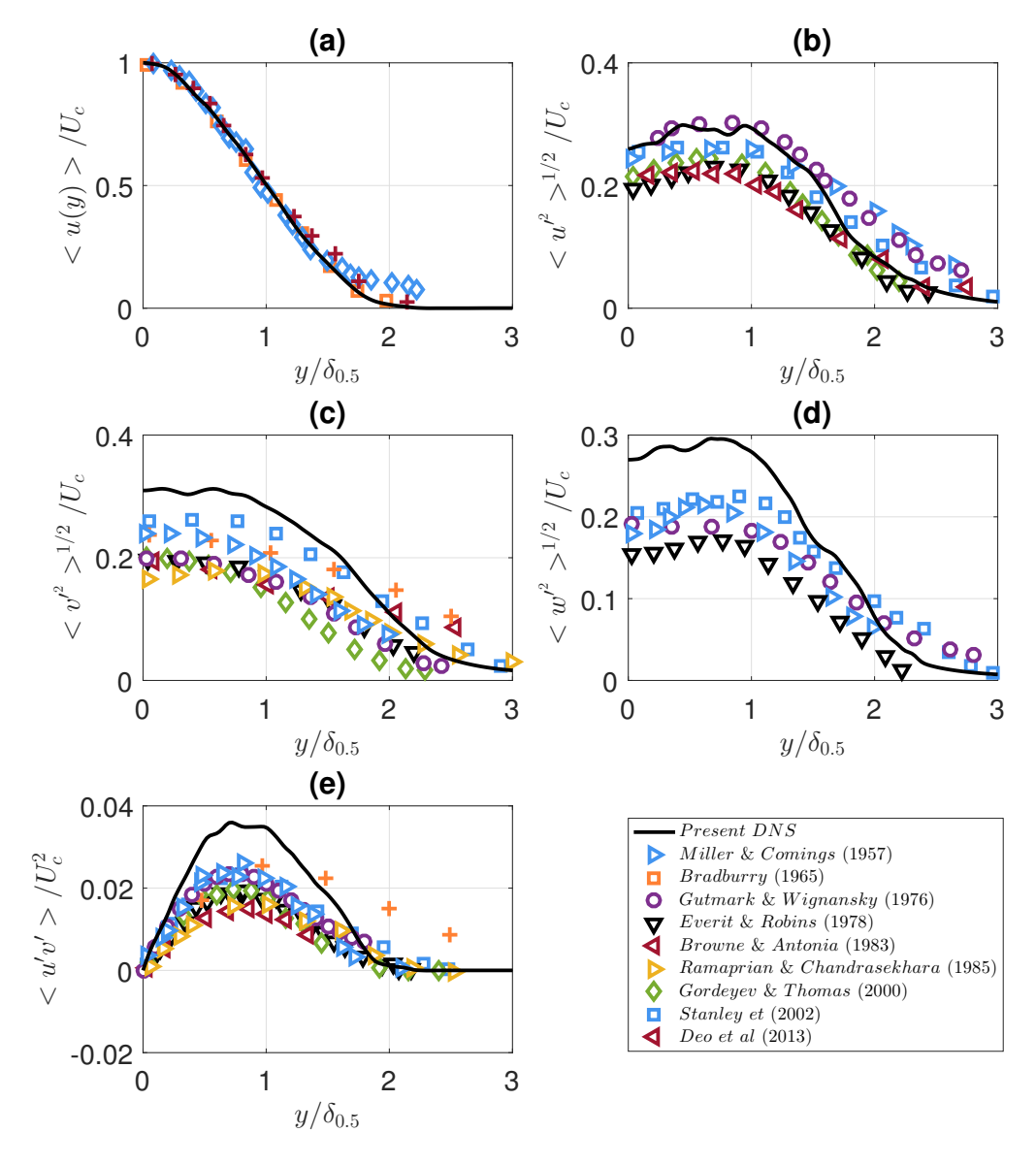


Figure 2: Transverse profiles of the Reynolds stress and mean velocity components at the fully turbulent far-field region of a Newtonian planar jet normalized as in the classical theory and comparison with experimental data. 4,5,10–13,19,22,25

4.2 Variable Density Jet

To assess the effects of temperature and density variations into the turbulence features two additional DNS, having a stream temperature two ($dT_1dT_2 = 2$) and four ($dT_1dT_2 = 4$) times higher compared to surrounding fluid, have been carried out. The simulations have been run until the self-similar state is achieved.

Figure 3 shows the same statistics obtained for the isothermal jet compared with the same calculated for the two variable density cases.

The mean velocity profiles, as illustrated in Figure 3a, collapse neatly on top of each other, indicating that a self-similar regime is achieved in all the direct numerical simulations. This observation suggests that the mean large-scale

quantities remain unaffected by the imposed temperature difference, at least within the range of parameters considered.

However, when examining the Reynolds stress profiles, a different trend becomes apparent. Although the three profiles are similar in shape, they do not collapse onto a single curve. Instead, there is a noticeable tendency for the magnitude of the Reynolds stresses to decrease as the temperature, and thus density, difference increases. This divergence suggests that, unlike the mean flow, the turbulence characteristics are sensitive to thermal effects. One plausible explanation for this behavior is the presence of baroclinic effects, which can act to dampen velocity fluctuations and thus reduce the intensity of turbulent stresses. The effect of temperature on turbulence and jet stability has been discussed in the literature, where increased core temperature can lead to greater flow stability and a reduction in turbulent fluctuations. This is noticeable in the energy spectra as well (Figure 4). Indeed, increasing the temperature ratio the energy present as high wave-numbers diminishes visibly.

Overall, these results highlight the complex interplay between thermal/density and hydrodynamic effects in turbulent jets. While the mean flow achieves self-similarity regardless of temperature difference, the turbulence structure, as reflected in the Reynolds stresses, is clearly influenced by baroclinic gradients.

The differences in density and temperature play a significant role in influencing the vorticity dynamics within the flow. Figure 5(b) presents the mean conditional vorticity magnitude profiles computed for two representative cases, namely $dT_1dT_2=2$ and $dT_1dT_2=4$. These profiles are evaluated to provide insight into how density variations affect the spatial distribution of vorticity across the interface between turbulent and non-turbulent regions.

On the horizontal axis, the distance from the turbulent/non-turbulent interface is shown as $\langle y \rangle_I$, normalized by the Kolmogorov length scale $\eta = (\nu^3/\varepsilon)^{1/4}$, which is calculated along the centerline of the jet. The coordinate $\langle y \rangle_I/\eta$ thus provides a non-dimensional measure of distance relative to the local smallest scales of turbulence. Negative values of this normalized distance $(\langle y \rangle_I/\eta < 0)$ correspond to the non-turbulent or irrotational region outside the turbulent core, while positive values $(\langle y \rangle_I/\eta > 0)$ correspond to the fully turbulent region within the jet. The point $\langle y \rangle_I/\eta = 0$ marks the location of the so-called irrotational boundary, an interface that separates the turbulent core from the surrounding irrotational fluid. In line with convention in previous studies, 7.24,27 the irrotational boundary is defined here as an iso-surface of vorticity magnitude, chosen to consistently capture the edge of the turbulent region.

The vertical axis reports the conditional mean vorticity magnitude, $\langle |\vec{\omega}| \rangle_I$, normalized by the ratio of the Kolmogorov velocity scale $u_{\eta} = (\nu \varepsilon)^{1/4}$ to the Kolmogorov length scale. This normalization ensures that the profiles are presented in a dimensionless form that facilitates comparison between different flow conditions. The shape of the vorticity magnitude profiles derived from these measurements is consistent with observations from previous literature.⁷

In the non-turbulent region, the vorticity magnitude remains close to zero, reflecting the near absence of rotational motion. However, a sharp rise in vorticity magnitude is observed just beyond the irrotational boundary, indicating the sudden onset of vorticity dynamics as the flow transitions into the turbulent region. Deeper into the turbulent core, the growth in vorticity magnitude stabilises as there is dynamic balance between vorticity production mechanisms and dissipative processes dominated by viscosity.

Despite the overall similarity in the shape of the vorticity profiles for the two configurations ($dT_1dT_2 = 2$ and $dT_1dT_2 = 4$), a clear difference is observed in their magnitudes within the turbulent region (see Figure 5b). Specifically, the peak vorticity magnitude for the $dT_1dT_2 = 4$ case is nearly twice that observed in the $dT_1dT_2 = 2$ case. This disparity is likely linked to baroclinic effects that become more pronounced at higher temperature/density differences. When pressure and density gradients are not aligned, a common occurrence in variable-density flows, a baroclinic torque is introduced, which can either generate or dissipate vorticity depending on the local configuration of gradients. In such situations, a "local shear layer" may form at the interface, contributing to enhanced vorticity dynamics.

The observed differences in the conditional mean vorticity magnitude profiles thus suggest that the cumulative effect of the baroclinic term is dissipative on average. This means that baroclinicity may act to suppress or redistribute vorticity depending on the local flow topology and thermodynamic gradients.

A more detailed and quantitative assessment of the baroclinic effects is beyond the scope of the current study and will be addressed in future work. In particular, further insight is expected to be gained through a comprehensive analysis of the enstrophy transport equation, which will help isolate the individual contributions of production, dissipation, and transport terms, including the baroclinic torque, within different regions of the flow.

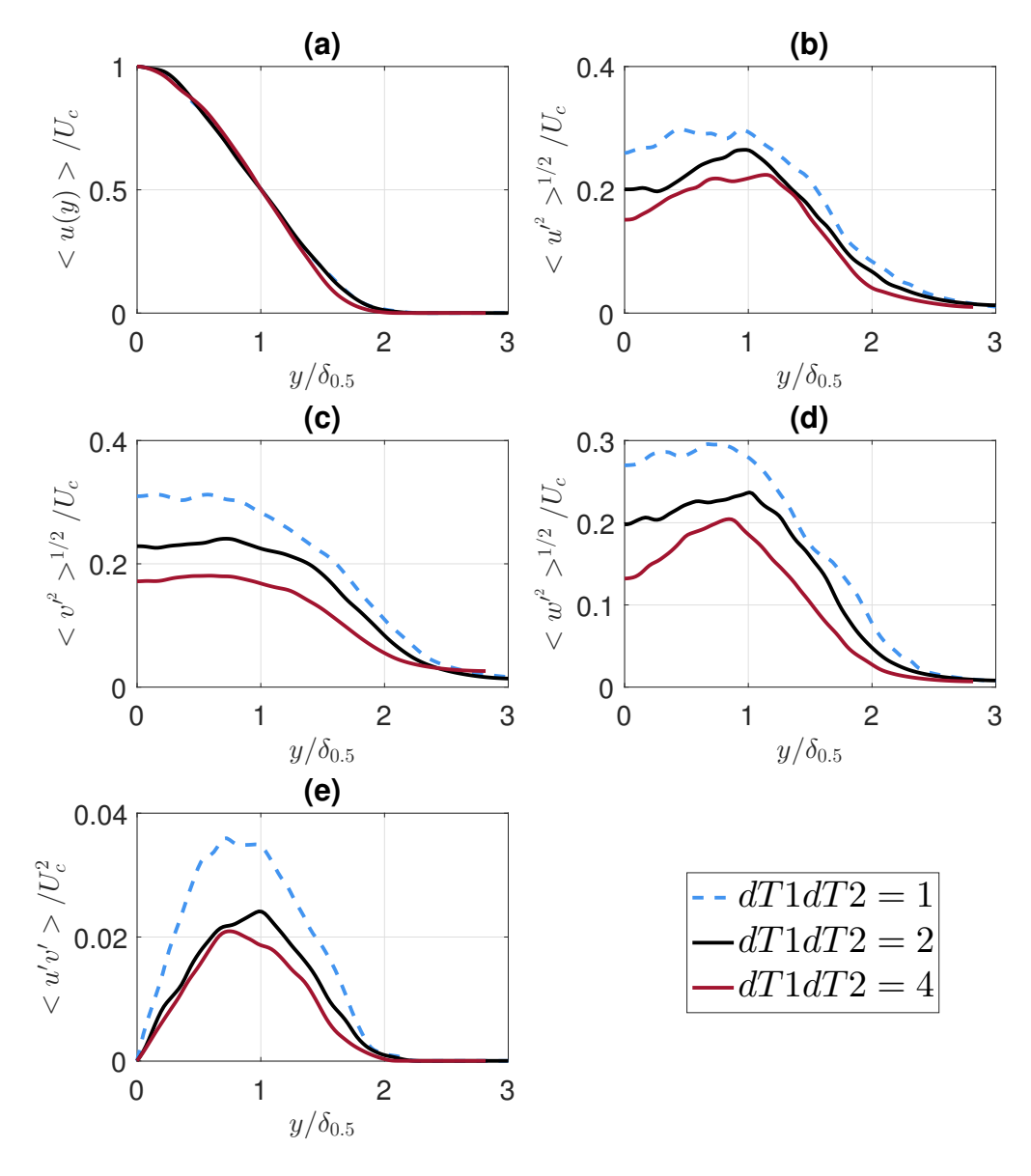


Figure 3: Transverse profiles of the Reynolds stress and mean velocity components at the fully turbulent far-field region of an isothermal jet and two variable density ones.

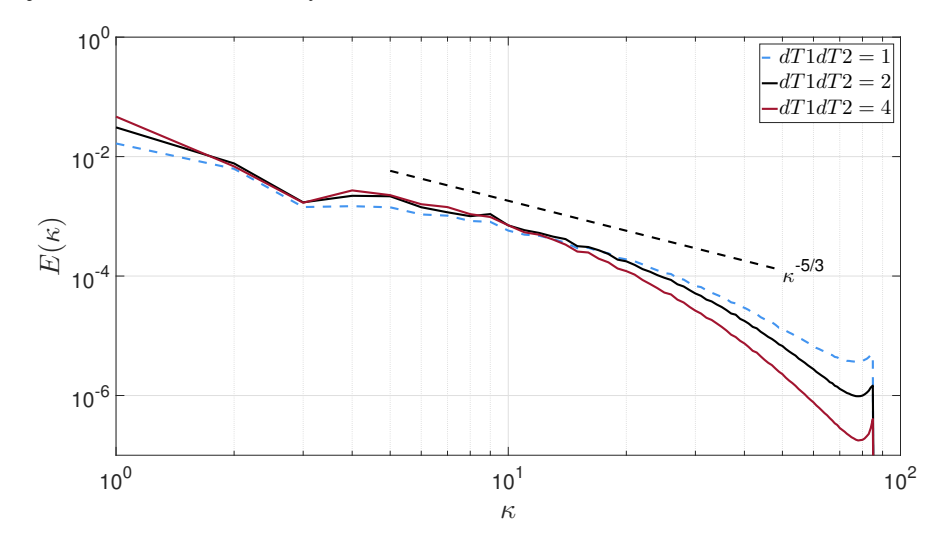


Figure 4: Three dimensional kinetic energy spectra $E(\kappa)$ from the isothermal jet simulation.

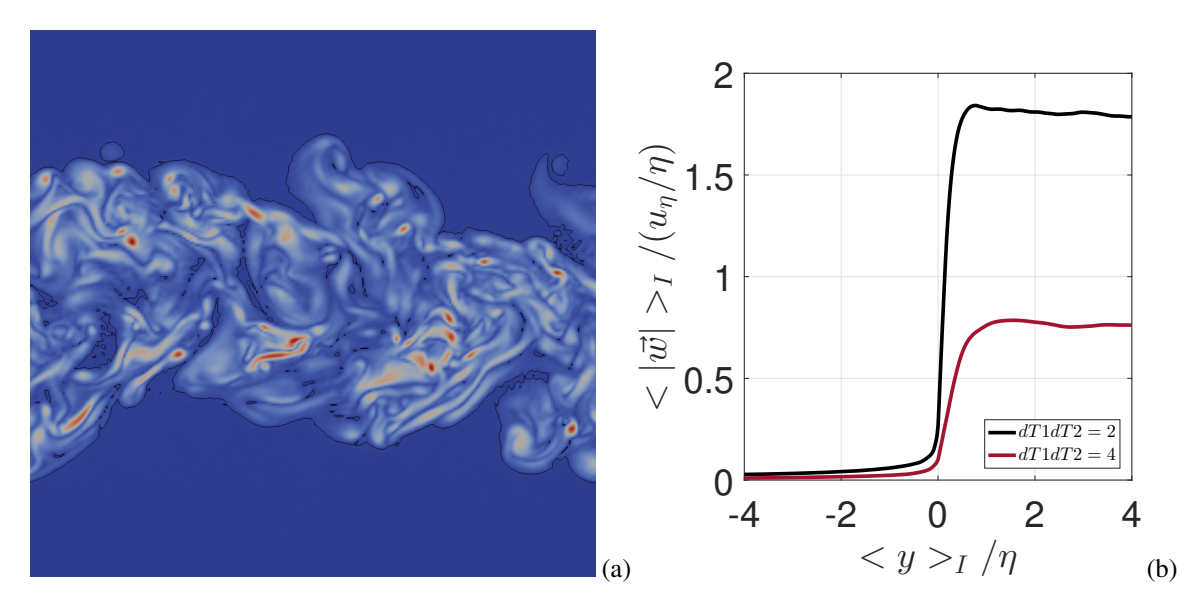


Figure 5: (a) Contours of vorticity magnitude from a DNS of a turbulent planar heated jet, at the far field fully develloped region; (b) Conditional mean profiles of vorticity magnitude $\langle |\vec{\omega}| \rangle_I$, in relation to the distance from the turbulent non-turbulent interface, y_I . The irrotational boundary is located at $y_I = 0$, while the non-turbulent and the turbulent regions are located at $y_I < 0$ and $y_I > 0$, respectively. All the quantities are normalised with the Kolmogorov micro-scale velocity and length scales, η and u_η , respectively, computed in the turbulent core region.

5. Conclusions

This work presented the development and validation of a low-Mach number direct numerical simulation (DNS). The solver was demonstrated to accurately resolve both incompressible and variable-density turbulent flows, capturing fine-scale turbulence and reproducing classical self-similar behaviours in isothermal jets.

Simulations across a range of temperature ratios revealed that while the mean velocity field retains self-similarity and is largely unaffected by thermal variations, the turbulence statistics are significantly influenced. As the temperature (and thus density) contrast increases, a clear reduction in Reynolds stresses and small-scale turbulent energy is observed, likely due to baroclinic damping effects. The conditional vorticity profiles further underscore these findings, showing enhanced suppression of rotational motion in cases with higher thermal gradients.

These results highlight the complex coupling between thermal and hydrodynamic fields in variable-density turbulent jets and underscore the importance of resolving both mean and fluctuating quantities for accurate physical understanding. Future work will focus on quantitatively analysing the baroclinic term in the enstrophy transport equation to further elucidate its role in turbulence modulation under supercritical conditions.

6. Acknowledgments

The present work was performed under the scope of activities at the Institute of Mechanical Engineering (IDMEC) and the Aeronautics and Astronautics Research Center (AEROG) of the Laboratório Associado em Energia, Transportes e Aeroespacial (LAETA), and was supported by the Fundação para a Ciência e Tecnologia, Portugal (Project doi: 10.54499/UIDB/50022/2020, 10.54499/UIDP/50022/2020 and 10.54499/LA/P/0079/2020).

References

- [1] J. H. Bae, J. Y. Yoo, and H. Choi. Direct Numerical Simulation of Turbulent Supercritical Flows with Heat Transfer. *Physics of Fluids*, 17(10):105104, 2005.
- [2] D. T. Banuti and K. Hannemann. The Absence of a Dense Potential Core in Supercritical Injection: A Thermal Break-up Mechanism. *Physics of Fluids*, 28(3), March 2016.
- [3] F. Battista, F. Picano, and C. M. Casciola. Turbulent Mixing of A Slightly Supercritical van der Waals Fluid at Low-Mach Number. *Physics of Fluids*, 26(5):055101, may 2014.

- [4] L. J. S. Bradbury. The Structure of a Self-preserving Turbulent Plane Jet. *Journal of Fluid Mechanics*, 23(01):31, September 1965.
- [5] L. W. B. Browne and R. A. Antonia. Measurements of Turbulent Prandtl Number in a Plane Jet. *Journal of Heat Transfer*, 105(3):663–665, August 1983.
- [6] P. Costa. Direct Numerical and Large-Eddy Simulations of Turbulent Variable-density Jets A Temporal Approach. Master's thesis, Instituto Superior Técnico, 2012.
- [7] C. B. da Silva, J. C.R. Hunt, I. Eames, and J. Westerweel. Interfacial Layers Between Regions of Different Turbulence Intensity. *Annual Review of Fluid Mechanics*, 46(Volume 46, 2014):567–590, 2014.
- [8] C. B. da Silva and O. Metais. On the Influence of Coherent Structures upon Interscale Interactions in Turbulent Plane Jets. *Journal of Fluid Mechanics*, 473:103â145, 2002.
- [9] D. W. Davis and B. Chehroudi. Measurements in an Acoustically Driven Coaxial Jet under Sub-, Near-, and Supercritical Conditions. *Journal of Propulsion and Power*, 23(2):364–374, March 2007.
- [10] R. Deo, M. Jianchun, and N. Graham. The Influence of Reynolds Number on a Plane Jet. *Physics of Fluids*, 20(7), July 2008.
- [11] K. W. Everitt and A. G. Robins. The Development and Structure of Turbulent Plane Jets. *Journal of Fluid Mechanics*, 88(3):563–583, October 1978.
- [12] S. V. Gordeyev and F. O. Thomas. Coherent Structure in the Turbulent Planar Jet. Part 1. Extraction of Proper Orthogonal Decomposition Eigenmodes and their Self-similarity. *Journal of Fluid Mechanics*, 414:145–194, July 2000.
- [13] E. Gutmark and I. Wygnanski. The Planar Turbulent Jet. *Journal of Fluid Mechanics*, 73(3):465–495, February 1976.
- [14] C. Lagarza-Cortes, J. Ramirez-Cruz, M. Salinas-Vazquez, W. Vicente-Rodriguez, and J. M. Cubos-Ramirez. Large-eddy Simulation of Transcritical and Supercritical Jets Immersed in a Quiescent Environment. *Physics of Fluids*, 31(2), February 2019.
- [15] L. B. Magalhaes, A. R. R. Silva, and Jorge M. M. B. Contribution to the Physical Description of Supercritical Cold Flow Injection: The Case of Nitrogen. *Acta Astronautica*, 190:251–260, January 2022.
- [16] A. Majda and J. Sethian. The Derivation and Numerical Solution of the Equations for Zero Mach Number Combustion. *Combustion Science and Technology*, 42(3-4):185–205, jan 1985.
- [17] F. May. Development of a DNS Code to Study Homogeneous Isotropic Turbulence for Incompressible and Variable Density Flows. Master's thesis, Instituto Superior Técnico, 2025.
- [18] W. Mayer, J. Telaar, R. Branam, G. Schneider, and J. Hussong. Raman Measurements of Cryogenic Injection at Supercritical Pressure. *Heat and Mass Transfer*, 39(8-9):709–719, jul 2002.
- [19] D. R. Miller and E. W. Comings. Static pressure distribution in the free turbulent jet. *Journal of Fluid Mechanics*, 3(1):1–16, October 1957.
- [20] N A. Okong'o and J. Bellan. Direct Numerical Simulation of a Transitional Supercritical Binary Mixing Layer: Heptane and Nitrogen. *Journal of Fluid Mechanics*, 464:1–34, aug 2002.
- [21] S. B. Pope. Turbulent Flows. Cambridge University Press, 2000.
- [22] B. R. Ramaprian and M. S. Chandrasekhara. LDA Measurements in Plane Turbulent Jets. *Journal of Fluids Engineering*, 107(2):264–271, June 1985.
- [23] F. Ries, P. Obando, I. Shevchuck, J. Janicka, and A. Sadiki. Numerical Analysis of Turbulent Flow Dynamics and Heat Transport in a Round Jet at Supercritical Conditions. *International Journal of Heat and Fluid Flow*, 66:172–184, aug 2017.
- [24] T. S. Silva, M. Zecchetto, and C. B. da Silva. The Scaling of the Turbulent/non-turbulent Interface at High Reynolds Numbers. *Journal of Fluid Mechanics*, 843:156–179, March 2018.

- [25] S. A. Stanley, S. Sarkar, and J. P. Mellado. A Study of the Flow-field Evolution and Mixing in a Planar Turbulent Jet Using Direct Numerical Simulation. *Journal of Fluid Mechanics*, 450:377–407, January 2002.
- [26] M. Zecchetto. *Universality and Scaling Relations for Turbulent/non-turbulent Interfaces in Free Shear Flows.* PhD thesis, Instituto Superior Tecnico, 2023.
- [27] M. Zecchetto and C. B. da Silva. Universality of Small-scale Motions Within the Turbulent/non-turbulent Interface Layer. *Journal of Fluid Mechanics*, 916:A9, 2021.